Evaluation of Ta-Co alloys as novel high-k EUV mask absorber

Devesh Thakare,[a,b,*] Meiyi Wu,[a,b] Karl Opsomer,[b] Qais Saadeh,[c] Victor Soltwisch,[c] Philipp Naujok,[d] Christophe Detavernier,[e] Davide Dattilo,[f] Markus Foltin,[f] Andy Goodyear,[g] Mike Cooke,[g] Annelies Delabie,[a,b] Vicky Philipsen,[b,*]

[a]KU Leuven Department of Chemistry, Celestijnenlaan 200 F, 3001 Leuven, Belgium
[b]imec, Kapeldreef 75, B-3001 Leuven, Belgium
[c]Physikalisch-Technische Bundesanstalt (PTB), Abbestr. 2-12, 10587 Berlin, Germany
[d]OptiX fab GmbH, Otto-Schott-Strasse 41, 07745 Jena, Germany
[e]Ghent University, Dept. of Solid-state Sciences, Krijgslaan 281 / S1, 9000 Gent, Belgium
[f]Süss MicroTec Photomask Equipment GmbH & Co. KG, Ferdinand-von-Steinbeis-Ring 10, 75447 Sternenfels, Germany
[g]Oxford Instruments Plasma Technology, Yatton, Bristol BS49 4AP, United Kingdom

Abstract:

Background: A plausible approach for mitigating the Mask 3-D (M3D) effects observed in EUV lithography is to replace the existing mask absorber with alternative materials. Absorbers with a high EUV extinction coefficient *k* allow lower Best Focus Variation (BFV) through pitch and reduced Telecentricity Errors (TCE).

Aim: To evaluate Ta-Co alloys as potential high-*k* mask absorbers from material suitability and imaging standpoint.

Approach: We study film morphology, surface composition, and stability of Ta-Co alloys in mask cleaning solutions and a hydrogen environment as present in the EUV scanner to assess the material suitability from an experimental aspect. Optical constants for three selected compositions, viz. TaCo, Ta_2Co, and $TaCo_3$ were determined from EUV angle-dependent reflectivity measurements. Next, utilizing rigorous simulation software, the imaging performance of Ta-Co alloys is evaluated and compared with the reference absorber. The recommended absorber thickness for Ta-Co alloy absorbers is based upon Normalized Image Log Slope (NILS) enhancement, Threshold to Size (TtS), and balancing of diffraction order amplitudes. A 10 nm line and space pattern with a pitch of 20 nm and 14 nm square contact holes with a pitch of 28 nm are used for the simulation study using High Numerical Aperture (NA) 0.55 EUV lithography process settings. The primary imaging metrics for thorough pitch evaluation include NILS, TCE, and BFV.

Results: The Ta-Co alloys exhibit a higher EUV extinction coefficient *k* compared to the currently used Ta-based absorber. TaCo and Ta_2Co demonstrate smooth surfaces and are stable in a hydrogen environment and in mask-cleaning solutions.

Conclusion: Ta-Co alloys allow for a reduction in M3D effects at lower absorber thickness compared to a 60 nm Ta-based reference absorber.

Keywords: EUV Lithography, EUV Photomasks, EUV Absorbers

*Address all correspondence to Devesh Thakare, devesh.thakare@imec.be and Vicky Philipsen, vicky.philipsen@imec.be

1 Introduction

Semiconductor devices have practically infiltrated almost every aspect of daily life, including education, entertainment, communication, transportation, and health. With the expanding reach of the Internet of Things, smart gadgets necessitate intelligently designed electronic systems. Applications involving machine learning, data science, outer space exploration, video games, and cryptocurrency demand immense computing power and memory. As a result, a resurgence

of interest in the field of semiconductors is observed in the global economy.[1] The semiconductor industry's desire to manufacture faster electronic circuits has driven transistor fabrication in the nanoscale range. Lithography is the key process in semiconductor manufacturing that enables the industry to achieve its goal. As deep ultraviolet 193 nm immersion lithography is approaching its printing limits, Extreme Ultraviolet (EUV) lithography has emerged as a savior to facilitate the patterning processes that are used in the production of smaller, faster, and high-performance transistors.

A photomask is an essential component of the lithography process that acts as a master copy of the patterns to be printed on the silicon wafer. In contrast to traditional lithography, pattern transfer in next-generation EUV lithography is performed with reflective optics rather than transmissive. A typical EUV mask consists of a Bragg reflector with a patterned absorber material on top of it. The state-of-the-art EUV masks use a Ta-based compound as bulk absorber material. The light-matter interaction of the EUV light source with the mask distorts the aerial image at the wafer level from its intended shape and position.[2] The main challenges associated with image formation at the wafer level are contrast fading (reduction in Normalized Image Log Slope (NILS)), pattern shift through focus (also known as Telecentricity Error (TCE)), and Best Focus Variation (BFV) through pitch. These effects are collectively termed as Mask 3-Dimensional (M3D) effects that can adversely affect production efficiency. The impacts of the interactions are considerable since the wavelength of the EUV light used in the lithography tool (13.5 nm) is substantially smaller than the absorber thickness and pattern size on the mask. Also, the oblique incidence is a strong contributor to the M3D effects. The optical constants of the absorber materials, namely the refractive index *n* and the extinction coefficient *k*, have a significant effect on the imperfections observed in the quality of an aerial image. Proper selection of absorber material and its thickness is expected to partially mitigate the M3D effects.[3] From an imaging standpoint, simulation studies have questioned the existing Ta-based material's efficacy as an EUV mask absorber for High Numerical Aperture (NA) 0.55 EUV lithography.[4] The necessity to fabricate smaller patterns with fewer defects will indisputably lead to stringent production specifications and intensify the challenges. This motivates exploring other materials as an alternative to the current Ta-based absorber.

Absorber materials are classified depending on their optical constants, viz. *n* and *k* values at EUV wavelength as high absorption, attenuated phase shifting, and vacuum phase matching (Fig. 1). The classification is based on the material's relative position in comparison to the current Ta-based absorber, which is marked red in Fig. 1. NILS, TCE, and BFV exhibit tradeoffs with *n* and *k*.[5] Low-n materials tend to produce higher NILS.[4],[5] High-k materials are expected to demonstrate a reduction in BFV.[5] Vacuum phase matching materials should be able to lower the TCE. [3],[5] Alloying enables modification of the optical properties, as well as the morphology, crystallinity, and stability, to meet the desired specifications of novel EUV absorbers.[3],[6] Ta's familiarity with the mask ecosystem makes it appealing to investigate Ta alloys. Single-layer Co has been previously investigated as a prospective EUV mask absorber.[7] Co has a high extinction coefficient. However, a single metal layer is prone to crystallization and has an impact on the mask line edge roughness, which in turn influences the printed Critical Dimension (CD).[3],[5] Alloying Ta with Co is expected to overcome this barrier. Stortelder et al. recently reported the compatibility of TaCo in EUV scanner conditions in the presence of hydrogen radicals.[8] A thermodynamic assessment of the Co-Ta system was reported by Wang P. et al.. [9] Nevertheless, so far, the structure and optical properties of Ta-Co alloy thin films and their dependence on the alloy's composition have not yet been extensively addressed in the literature for EUV lithography.

The absorber material and the Multi-Layer (ML) mirror component of a EUV mask are the major contributors to M3D effects.[10] Therefore, it is required to investigate the imaging performance of a novel EUV absorber in combination with the existing industry-standard Mo/Si ML mirror. A fast and cost-effective approach to analyze the imaging performance is to use lithography simulation software that emulates the specific EUV tool settings.

Additionally, it is also important to shed some light on patterning challenges involved with novel EUV mask absorbers. In general, most of the studies that have proposed novel EUV mask absorbers belong to the noble materials category, which are difficult to pattern.[3],[8] Also, it is challenging to pattern ferromagnetic materials like Co because they do not produce easily-removable volatile byproducts.[11] Although dry etch techniques that include Reactive Ion Etch (RIE), such as Cl_2/Ar plasma etch, have been developed, the halogen reaction with Co to form metal chlorides is not volatile enough below the temperature of 200°C for practical applications.[12],[13] Refraining from temperatures above 150°C is suggested for EUV photomasks to prevent Mo/Si ML mirror damage.[14] In the literature, we come across organic chemical vapor etch of Co using energetic noble gas atoms under low temperatures.[15] In this study, we explore etch of TaCo alloys along with prospective hard mask materials such as SiO_2 and Si_3N_4.

This paper presents an experimental and theoretical exploration of Ta-Co alloys as potential high-k mask absorbers. First, we study film morphology, surface composition, and chemical stability by means of experiments. Next, we discuss the imaging performance through aerial image simulations. Finally, we conclude the feasibility of the novel mask absorber vs. the available Ta-based reference.

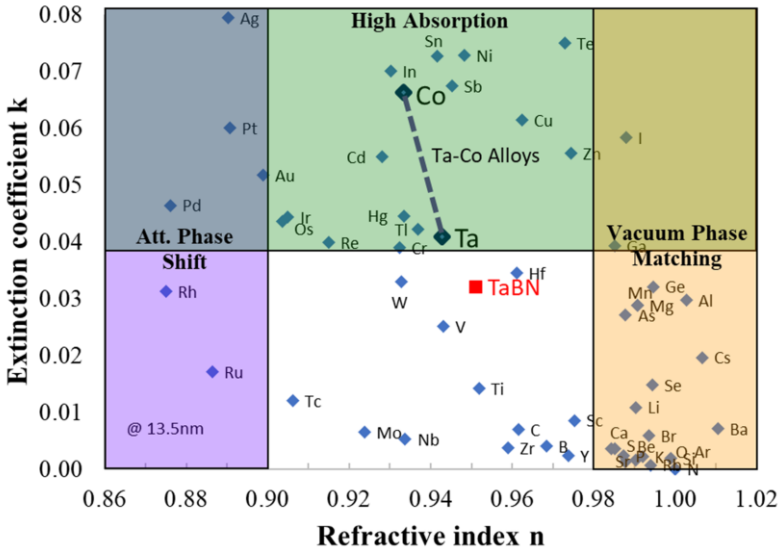

Fig. 1 EUV material classification in the EUV *n* & *k* range,[16] reference Ta-based absorber highlighted in red. The dashed line connecting Ta and Co symbolizes the Ta-Co alloys' expected *n* and *k* values.

2 Methodology

2.1 Experimental Methods

Based on the Ta-Co binary phase diagram (Fig. 2), three compositions of Ta-Co alloys were selected for the investigation, namely TaCo, Ta_2Co, and $TaCo_3$. The Materials Project's online phase diagram tool was utilized to identify stable Ta-Co alloy phases. The Materials Project is

an open-access database for materials research developed by the Lawrence Berkeley National Laboratory (Berkeley Lab) and the Massachusetts Institute of Technology (MIT).[17] The tool uses Density Functional Theory (DFT) calculations to generate compositional and phase diagrams.

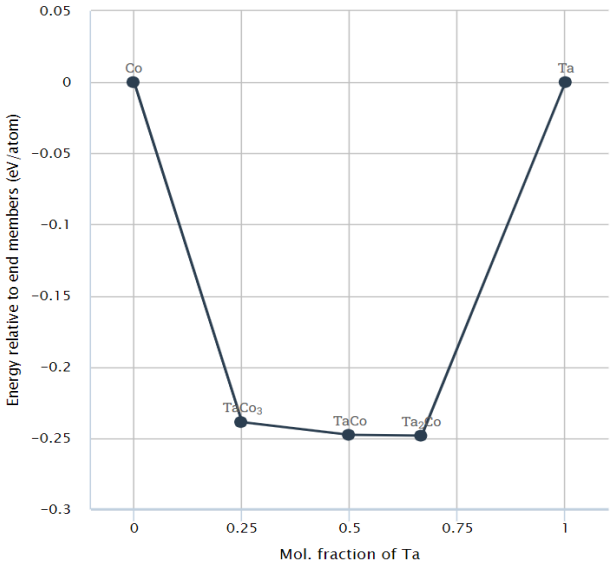

Fig. 2 Predicted stable Ta-Co alloys using phase diagram app by Materials Project [17], [18] based on which the Ta-Co alloy compositions that will be investigated are chosen.

2.1.1 Ta-Co alloy thin films deposition

For experimental evaluation, Ta-Co alloy films with a thickness of 30 nm each were deposited on 300 mm Si substrates. Ta_xCo_y alloy films were deposited by DC magnetron sputtering as periodic nano-laminates of Co and Ta films on 300 mm Si wafers with a 0.35 nm thickness of one Ta_xCo_y period. The Ta:Co ratio was tuned by adjusting the relative deposition time of Ta and Co layers, respectively. Due to the extremely thin single-layer thickness, full intermixing between the materials is expected. Each composition was deposited with two variations: one with a Ru underlayer of 3 nm on the Si substrate and another directly on the native Si oxide, without the Ru underlayer. In addition to the alloys, pure Ta and pure Co thin films with similar thicknesses were also studied.

2.1.2 Ta-Co alloy thin films morphology

A novel EUV absorber should be either amorphous or nanocrystalline.[3],[7] Therefore, In-Situ X-Ray Diffractometry (IS-XRD) was used to study thin film morphology and its stability over the temperature range of 25 °C to 600 °C. The 2θ scattering angle was varied from 30° to 50° to detect any possibility of crystallization over the temperature range. Cross-section Transmission Electron Microscopy (TEM) was used to verify the morphology of these thin films. The elemental composition in the bulk and on the surface was determined using Energy Dispersive X-ray Spectroscopy (EDS) in Scanning TEM (STEM). The recommended surface roughness specification for novel EUV mask absorbers is below 0.3 nm Root Mean Square (RMS).[3] Atomic Force Microscopy (AFM) was employed to verify the surface roughness of the samples.

2.1.3 Ta-Co alloy optical constants determination

To enable the determination of the optical constants, angle-dependent EUV reflectivity (EUVR) measurements were conducted in the EUVR beamline in the PTB's own storage ring,

the Metrology Light Source (MLS). Information on the EUVR beamline can be found in Ref..[19] The configuration excluding a Ru underlayer was considered for these measurements.

Later, using the genetic global optimization algorithm Differential Evolution (DE),[20],[21] the EUVR data were entered in an inverse-problem primarily targeting the simultaneous determination of *n* and *k*.[22] The inverse-problem was initialized with a stratified four-layer (on a substrate) model. Descendingly, the model presupposes a carbonaceous contamination layer, followed by an oxidation layer on top of the alloy deposition, followed by the substrate's native oxide. For the three alloyed samples, merely the optical constants of the main deposited layers and the geometrical characteristics of each model were optimized. The optical constants of the carbonaceous layer, the substrate, and its native oxide were fixed in the optimization, with the values of the first two taken from the CXRO's database (The Center for X-ray Optics, Berkeley) and the latter from Andrle et al..[23],[24] To reduce the dimensionality of optimization and to facilitate parametrization of the alloyed samples, the oxide's optical constants were estimated using the independent atom approximation from the optical constants of the elemental samples.[19]

The optimization targets minimizing the residual between the measured and the simulated data. The residual is weighted with the experimental uncertainties using the following ubiquitous objective function:

$$\chi^2 = \sum_{i=1}^{m} \left(\frac{R_m^{simulated} - R_m^{measured}}{Absolute\ Uncertainty_m} \right)^2 \qquad \text{Equation 1}$$

where m denotes the measurement's point index and $R^{measured}$ denotes the measurement's experimental data. $R^{simulated}$ is the simulated model's reflectivity.

The simulated reflectivity is calculated using Parratt's formalism coupled with Névot-Croce[25],[26] terms to compensate for the effects of interfacial imperfections for every EUVR data set. Upon reaching a quasi-stable solution, optimization was assumed to reach convergence.

2.1.4 Cleaning and durability test

Another important aspect of a prospective absorber is to withstand the cleaning conditions. EUV masks are expected to withstand more than 100 cleaning cycles with little to no influence on lithographic performance.[27] To assess the durability of Ta-Co alloys, sample coupons of 2 cm x 2 cm of each composition were submerged separately for 24 hours in the beakers containing the solution. The stability of these materials was studied in mask cleaning solutions with a wide range of pH viz. DIW (De-Ionized Water, pH 5.7), 1% NH_4OH (Ammonium Hydroxide, pH 11.4), and 0.2-0.5% TMAH (Tetramethylammonium Hydroxide, pH 12.8). These are common industry standard solutions used for mask cleaning. Analysis with X-Ray Reflectivity (XRR) using Cu Kα X-ray was performed to detect possible thickness or roughness changes after submersion in a cleaning solution. An additional pristine sample was kept aside to be used as a reference. In addition, the TaCo composition of the alloy was chosen for a more thorough analysis following the beaker tests. This involved automated cleaning inside the "MaskTrack*PRO*" cleaning tool of the full 300 mm wafers coated with 30 nm TaCo thin film. XRR and AFM measurements were performed after finite cleaning cycles to study the impact of cleaning on TaCo thin films. In a EUV scanner operation, the mask is exposed in a hydrogen environment to maintain self-cleaning conditions for the sensitive EUV mirrors[28] by preventing it from carbon contamination.[29] Ta-Co alloy samples were exposed to hydrogen radicals for 24 hours to test their stability. The radicals were generated by a heated tungsten filament in the "Hydrogen Cleaner" tool manufactured by EUVTech.[30] Rutherford Back

Scattering (RBS) analysis was performed on both the reference and exposed samples to determine a possible stoichiometry change resulting from hydrogen-induced outgassing. The surface oxide thickness was measured at different moments spaced over a year to assess the long-term stability of Ta-Co alloy thin films. These samples were stored in the lab environment of optiXfab, and XRR technique was used to determine the surface oxide thickness.

2.1.5 Ta-Co alloy Etch study

Finally, the plasma etch rates of TaCo, Ta, Co, Si_3N_4, SiO_2, and Ru layers were evaluated to understand the etch mechanism and to study the selectivity of TaCo over Ru (the typical underlayer) and TaCo over Si_3N_4 or SiO_2 (potential hard mask layers, to be used during absorber pattering process). The metal layers (30-50 nm thick) were deposited onto 100 nm SiO_2 on Si wafers. Thickness measurements, pre-etch, and post-etch, were carried out using a Woollam M-2000 Spectral Ellipsometer. Four-point probe resistance measurements were also carried out to confirm measured metal thicknesses. Samples were etched using an Oxford Instruments Plasma Technology PlasmaPro100 with Cobra300 Inductively Coupled Plasma (ICP) source and Electrostatic Chuck (ESC). Sample pieces (1 cm x 1 cm) were bonded to a Si_3N_4 coated Si carrier wafer to provide good thermal contact. Si_3N_4 coating of the Si carrier wafer was preferred since this mimicked one of the proposed mask layers. At 1 kW ICP, 20 mTorr, 80°C, and 10 Torr Helium wafer cooling, Cl_2/Ar etch recipe (20 sccm : 80 sccm (standard cubic centimeters per minute)) was employed.

2.2 Simulation Methods

The S-Litho EUV software by Synopsys was used to assess the imaging performance of absorber materials. S-Litho EUV runs rigorous Electro Magnetic Field (EMF) simulations that take into account mask topography as well as the optical properties of the mask materials. The imaging performance of Ta-Co alloys was compared with the current industry reference Ta-based absorber with a thickness of 60 nm for a high-NA 0.55 lithography system. The EUV scanner setup in the simulator employs a 20% central obscuration in an anamorphic projection mirror and Chief Ray Angle at Object (CRAO) of 5.355^o for an EUV light source having a wavelength of 13.5 nm.[31] The Mo/Si ML mirror mask model utilized during the simulations is as described by Makhotkin et al..[32] The experimentally determined optical constants *n* & *k* of Ta-Co alloys were used to define the absorber stack. This simulation study is focused on dark field Line and Space (LnS) patterns having a target CD of 10 nm with a 20 nm pitch (10 nm P20) and square Contact Holes (CH) arrays having a target CD of 14 nm with a 28 nm pitch (14 nm P28), which is also an industry goal by the year of 2028.[33] The orientation of LnS is either horizontal, i.e., orthogonal to the CRAO plane, or vertical, i.e., parallel. At the wafer level, the mask pattern is represented by an intensity distribution of light, known as an aerial image. The aerial image intensity level at which the target CD of a feature is measured is referred to as the Threshold to Size (TtS). It indicates the amount of exposure dose necessary to print on target, with a higher threshold implying a lower dose requirement.[3] NILS is the most important parameter for the evaluation of aerial image quality. It is evaluated at the TtS. Fluctuations in an illumination dose cause uncertainty in the position of a pattern on the wafer; the higher the NILS, the lower is the impact of dose fluctuations, and hence the lower is the defectivity.[34] NILS is influenced by the mask topography and material's optical constants (*n* & *k*) and thickness, the mask feature width (mask bias), and illumination source shape. This results in multivariable optimization and increases complication.

The thickness optimization is the first step in the simulation study. A Telecentric Sigma Point Source (TS-PS) is used as an illumination source during this step. For a TS-PS, NILS remains constant as a function of focus[35], which eliminates the necessity of an extra variable

(focus), resulting in faster simulations. The TS-PS illumination chosen for this simulation study corresponds to the smallest pitch that needs to be printed at the wafer level. The telecentric sigma can be calculated for equal lines and space patterns as given in Eq. 2 and for contact holes as given in Eq. 3. The trench width on the mask is varied in small steps (± around CD) to find the appropriate bias. The trench represents the absorber-free region of the EUV mask. For each combination of the absorber thickness and mask trench width, the TtS value that prints the target CD is calculated, and the corresponding NILS is reported. The combination of mask trench width and thickness that results in the maximum NILS is used for the evaluation, and the corresponding TtS is extracted. The main criteria for choosing the optimized absorber thickness are NILS, TCE values of <=10 mrad, and the ratio of the ±1st diffraction orders to the 0th diffraction order is close to 1 with a minimum phase difference. These diffraction order conditions improve the contrast, which benefits NILS.[36] Mesilhy et al.[37] observed that at sub-11 nm, the diffraction characteristic is governed by the waveguide effect, and, therefore, suggests focusing on *n*, *k*, and thickness versus transmission and phase. The results of our preliminary simulations also support the idea of improving EUV imaging metrics as a function of optical properties and thickness of the absorber with the inclusion of an illumination source. A separate paper will discuss the detailed reasoning and methods employed for determining the optimized absorber thickness.[38]

$$Telecentric\ \sigma\ for\ LnS = \frac{\lambda}{2\ NA\ P} \qquad \text{Equation 2}$$

$$Telecentric\ \sigma\ for\ CH = \frac{\lambda}{\sqrt{2}\ NA\ P} \qquad \text{Equation 3}$$

where λ denotes the wavelength of the illumination, *NA* is the numerical aperture, and *P* is the pattern pitch.

A smaller value of TtS results in larger NILS at a constant image slope, but consequently, it results in a larger exposure dose. To address this tradeoff, another metric known as Throughput Criterion (TpT) (Eq. 4) was taken into account.[39] It is an indicator that reflects a good balance between NILS and TtS. This additional criterion is used to narrow the absorber thickness range while determining the optimum absorber height.

$$Throughput\ Criterion\ (TpT) = NILS\sqrt{TtS} \qquad \text{Equation 4}$$

The evaluation metrics NILS, TCE, BFV, and TtS have a strong dependence on the choice of illumination. Franke et al.[35] suggest using either an inner half leaf or an outer half leaf-shaped dipole to observe an increment in NILS for Ta-based absorbers. Similarly, a two-dimensional incision resulting in quarter poles for quasar illumination is also recommended for contact holes. The scope of this paper is limited to a study of the imaging performance with a Leaf Shape Dipole (LDP) for the LnS pattern and a Full Quasar Pole (FQP) for the CH pattern. The illumination sources are optimized for the smallest pitch (Fig. 3).

Once the optimized absorber thickness is fixed, the next step is to perform a through-pitch simulation. For an illumination source optimized to the smallest pitch, wafer focus is varied along with the mask trench width to maximize the NILS. The TtS and best focus corresponding to the maximal NILS is extracted and used to calculate a proper mask bias for larger pitches that can print to the target CD with a tolerance level of +/-10%. Evaluation metrics, viz. NILS, TCE, and BFV of Ta-Co alloys are then compared with the reference Ta-based absorber with a thickness of 60 nm.

A NILS value greater than 2 is considered reliable for an effective pattern transfer.[40] TCE (also known as pattern shift through focus), expressed in mrad or nm/um, signifies a feature's lateral pattern shift as a function of focus. Mask-induced pattern shift through focus is a

consequence of the CRAO plane not being completely parallel to the feature orientation, causing an imbalance in the +1 and -1 diffraction order intensities. This is especially visible for horizontal features in any slit position and for vertical features in off-central slit positions.[31]

To evaluate the focus behavior through pitch, we varied the LnS pitch from 20 nm to 40 nm with an increment of 4 nm, whereas the CH pitch was 28 nm, 32 nm, 36 nm, 42 nm, and 56 nm. The focus value that yields a maximum NILS is considered the best focus for that specific pitch. The difference between the maximum and minimum value of the best focus through pitch is expressed as the best focus variation (BFV). The BFV should also be as small as possible to print the different patterns with the largest overlapping process window.

High NA EUV lithography is targeting a total focus budget of 35 nm.[41] A 10 mrad TCE translates to a 1 nm pattern shift per 100 nm of defocus that can result in Edge Placement Errors (EPE). Thus, the TCE should be as low as possible. Since the overlay error induced due to TCE can be only partially corrected, van Setten et al.[31] suggest that the mask-driven contribution should be kept under 20 mrad. The M3D-induced overlay error can be calculated from TCE and focus budget (Eq. 5).[31] An overlay control of 1.1 nm or below is targeted for high-NA applications.[42] For example, 10 mrad TCE translates to a 0.175 nm (10 mrad x 0.035µm/2) M3D-induced overlay error. This would mean that the mask is responsible for consuming ~16% of the overlay budget. According to van Setten et al.,[31] TCE, limited to 10 mrad, should not substantially influence the overlay budget. Therefore, this study aims to target a TCE of 10 mrad or below for the smallest pitch.

$$M3D\ induced\ overlay\ =\ TCE\ x\ Focus\ Budget\ half\ range \quad \text{Equation 5}$$

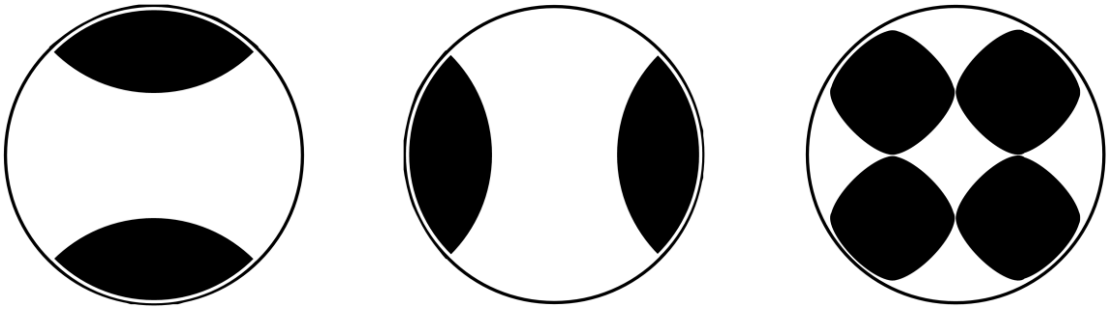

LDP for horizontal LnS (a) | LDP for vertical LnS (b) | FQP for square CH (c)

Fig. 3 Illumination source shapes used for simulations (a) leaf shape dipole (LDP) for horizontal LnS (b) LDP for vertical LnS (c) full quasar pole (FQP) for CH in a square array pattern

3 Results and Discussion

3.1 Experimental Results

In this section, we will go through the results and observations obtained from each experiment on Ta-Co alloy films and discuss them one by one.

3.1.1 Verifying the alloy composition.

First, the composition of the alloys was verified through RBS. The atomic content of Ta and Co atoms in each composition (as deposited) is shown in Fig. 4. The overall uncertainty in Ta

atom measurement is less than $3x10^{15}$ atoms/cm². The overall uncertainty in Co atom measurement is less than $4x10^{15}$ atoms/cm². Therefore, we can state that the observed concentration is close to what was anticipated. RBS reveals that the sample coupon of Ta-Co alloy 1:1 composition is actually slightly Ta rich, indicating the stable phase of Ta_7Co_6 as observed in Fig. 5. This phase has been referred to as TaCo throughout this paper for the sake of simplicity. The position of the three phases, TaCo, Ta_2Co, and $TaCo_3$, is highlighted with red arrows in the Ta-Co alloy phase diagram (Fig. 5). We can infer that these are stable phases based on the locations of the arrows in the phase diagram.

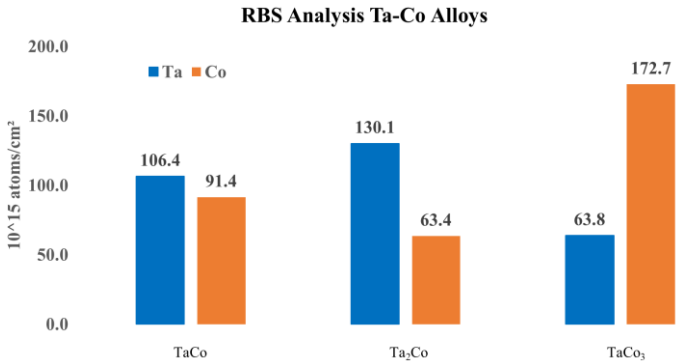

Fig. 4 RBS analysis of atomic content of Ta and Co of Ta-Co alloys

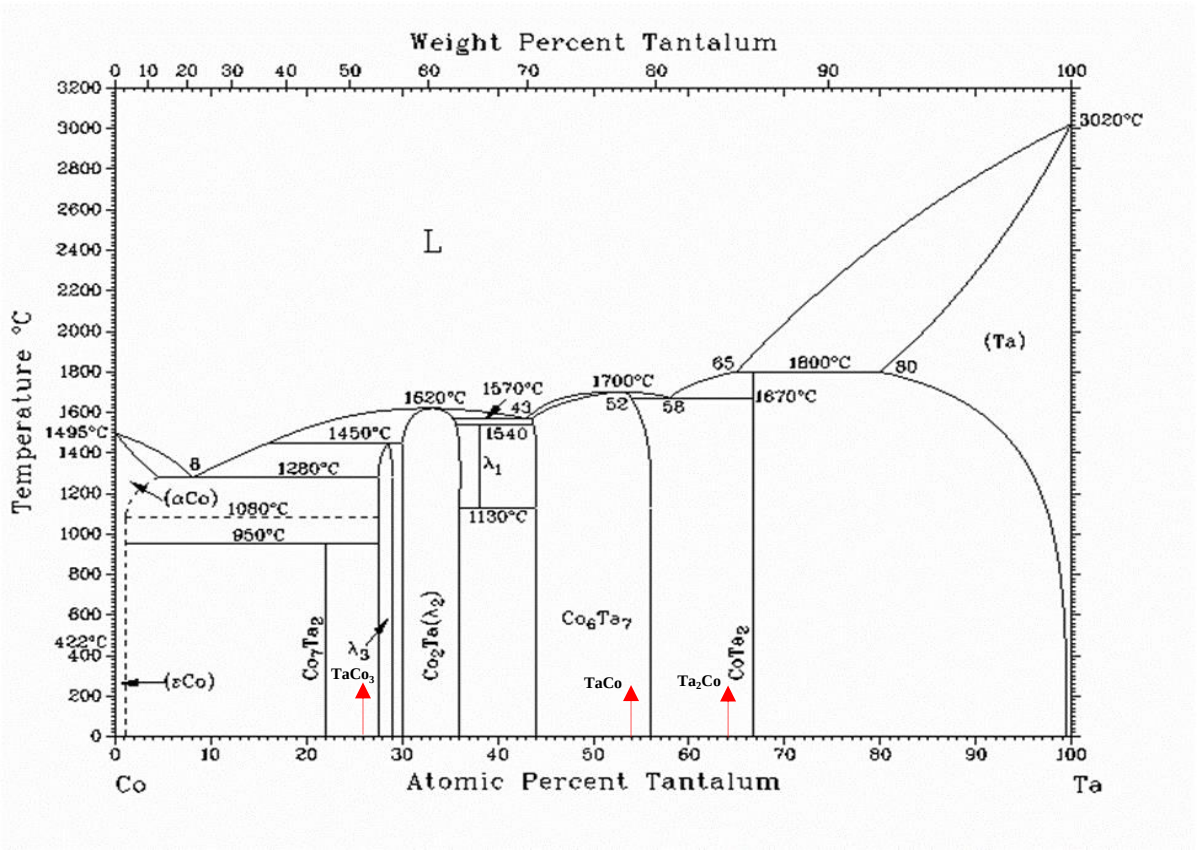

Fig. 5 Ta-Co, binary phase diagram, indicating the three Ta-Co alloy composition's position with red arrows (adapted) [43]

3.1.2 IS-XRD and temperature stability

A novel EUV absorber should be either amorphous or nanocrystalline in nature and stable during the mask fabrication steps and scanner operation. To determine if crystallization occurs,

we analyzed the phases of the alloys and their stability across a wide temperature range with in-situ XRD.

First, we investigate the stability of the Ta-Co alloys with and without a Ru underlayer. IS-XRD analysis found no evidence of crystalline Ta-Co phase development or silicide formation for all Ta-Co alloys (Fig. 6). As a result, all Ta-Co alloys under consideration here are amorphous and inherently thermally stable up to 600°C. Ru-silicide formation (Ru_2Si_3) is expected on Si (on cleaned Si (100)) from 450°C.[44] However, in our measurements, Ru silicide formation is not observable. The probable reason that Ru-silicide is not detected is because the 3 nm Ru layer is very thin and covered by large X-ray scattering atoms (Ta, Co) in a thicker layer (30 nm) on top of it. Also, some low-density Ru-oxide formation may occur from this thin layer at the Ru/Si interface (based on the presence of a small oxygen peak at the Ru/Si interface in the EDS-STEM line scan (see Fig. 8 b in next Sec. 3.1.3). The oxidation of Ru could affect the extent of Ru and Si interdiffusion when temperatures of silicide formation are reached. The interplay of all these factors will impact the XRD results in which diffraction peaks are visually absent. Thus, we cannot be conclusive about Ru-silicide formation based on these XRD results.

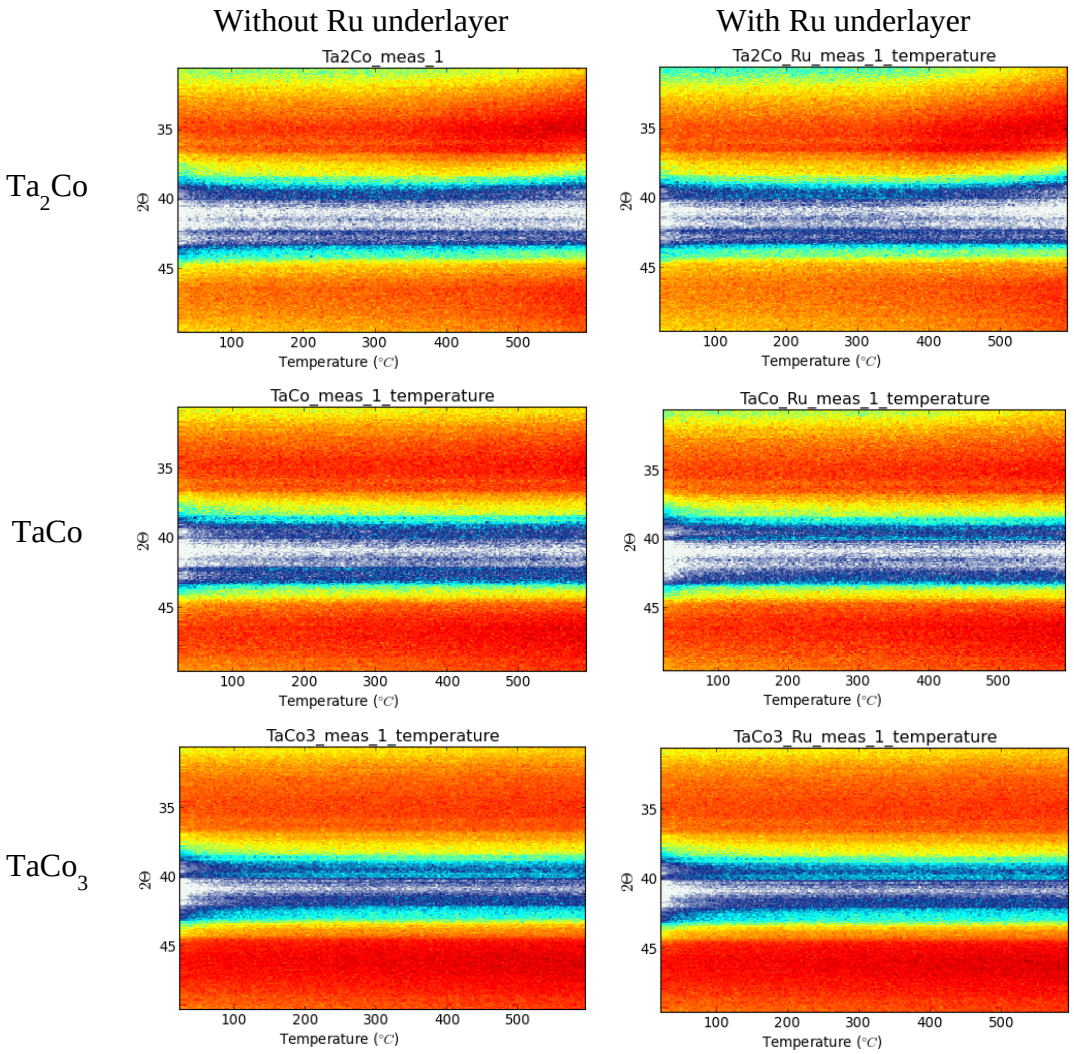

Fig. 6 In-situ XRD (IS-XRD) spectra of Ta_2Co, TaCo, and $TaCo_3$, with and without Ru underlayer over a range of temperatures. The intensity scale is displayed as a pseudo-color map, with white indicating the lowest intensity, blue intermediate level, and red representing the maximum intensity.

Next, we examined the stability of the pure Co and Ta metals without the Ru underlayer. IS-XRD analysis in Fig. 7(a) revealed the Co-silicide phase formation sequence from Co[45] to cubic CoSi[46] at 500°C and finally to FCC $CoSi_2$ [47] at 575°C.[48] The formation of Co_2Si preceding the CoSi around 425°C cannot be ruled out due to closely matching diffraction peak positions. The formation of the Ta silicide phase is less apparent. The peak detected about 34° of 2θ in Fig. 7(b) corresponds to Ta in the as-deposited film.[49] The bending observed in the diffraction peak towards lower 2θ from ~300°C onwards indicates a structural change. The speculated causes include Ta-Si interdiffusion and/or trapped oxygen from the chamber in the Ta layer forming an oxide. The dotted lines in Fig. 7(b) depict the expected peaks for Ta_3Si_5.[50] Instead of a sharp peak, the broad nature of the peak observed at 500°C makes it difficult to distinguish the formation of either Ta silicide or Ta oxide in the given temperature range. As stated earlier, EUV photomasks are rarely subjected to temperatures beyond 150°C to avoid Mo/Si ML mirror degradation.[14] In a real case scenario, a 3 nm of Ru capping layer is expected to act as a barrier between the absorber and the Mo/Si ML mirror. Thus, Ta or Co silicide formation is insignificant for the intended application.

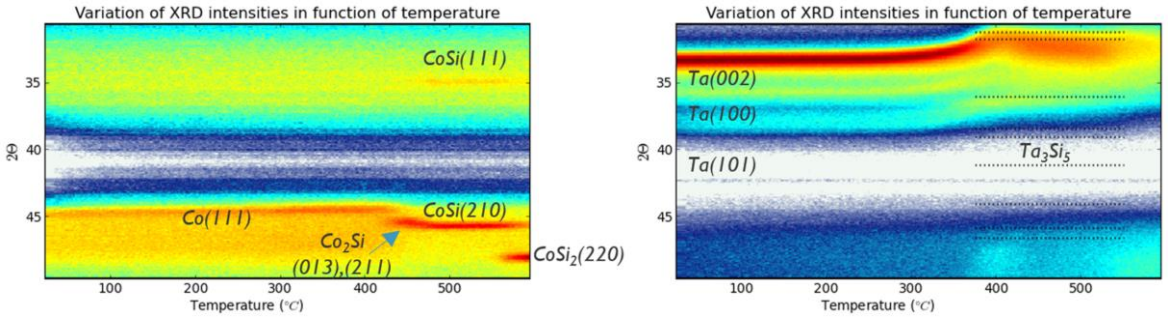

(a) (b)

Fig. 7 In-situ XRD (IS-XRD) spectra of (a) Co and (b) Ta.

3.1.3 TEM and EDS-STEM analysis

TEM images of Ta-Co alloys confirmed their amorphous nature as well as a homogeneous bulk composition (Fig. 8(a)). In addition, TEM reveals the presence of a top oxide layer with an estimated thickness in the range of 2-3 nm due to oxidation of the alloys during air exposure. Ta segregation with the formation of a Ta-rich oxide top layer was reported for the TaCo and Ta_2Co alloys, according to EDS-STEM (Fig. 8(b)). In contrast, Co segregation with the formation of a Co-rich oxide top layer was observed in the case of the $TaCo_3$ alloy. Furthermore, the O-content in the bulk of the Ta-Co alloy increases with the Co-content of the Ta-Co alloy, from close to zero for Ta_2Co up to almost 10% for $TaCo_3$. The Si's 'K' and Ta's 'M' EDS peaks are close in energy,[51] and they were challenging to deconvolute during quantification, which may be the cause of the Si signal appearing in the bulk region of the EDS spectrum (Fig. 8 (b)).

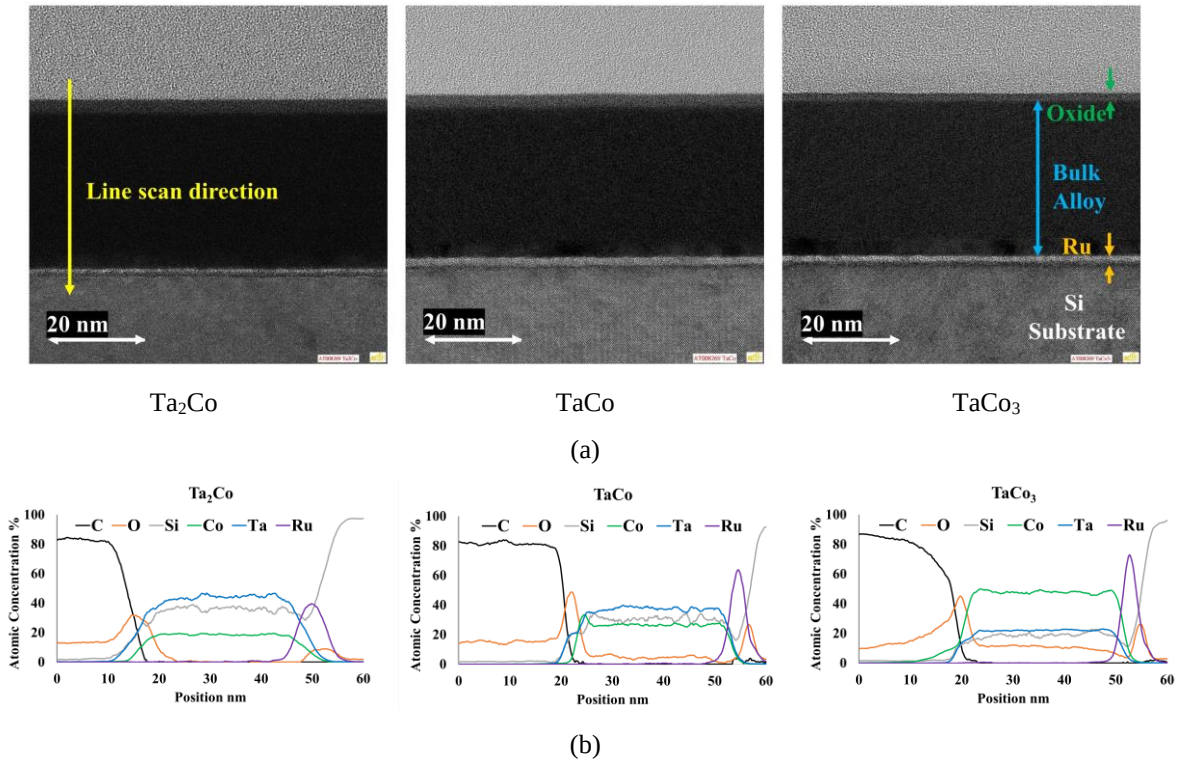

Fig. 8 (a) cross-section TEM of Ta-Co alloys (b) EDS-STEM line scan along the arrow in the TEM image

3.1.4 Surface roughness

Next, we investigated the surface roughness of the Ta-Co alloys. Fig. 9 depicts the AFM images and RMS value of the surface roughness as measured by AFM over an area of 1x1 μm^2. All three Ta-Co compositions exhibit smooth surfaces, and the RMS value remains within the specified limits for EUV mask absorbers (below 0.3 nm RMS).[52] On the other hand, the single metal surfaces are clearly rougher with an RMS value greater than 0.3 nm due to their crystalline nature. Thus, it is evident that the composition strongly influences surface roughness.

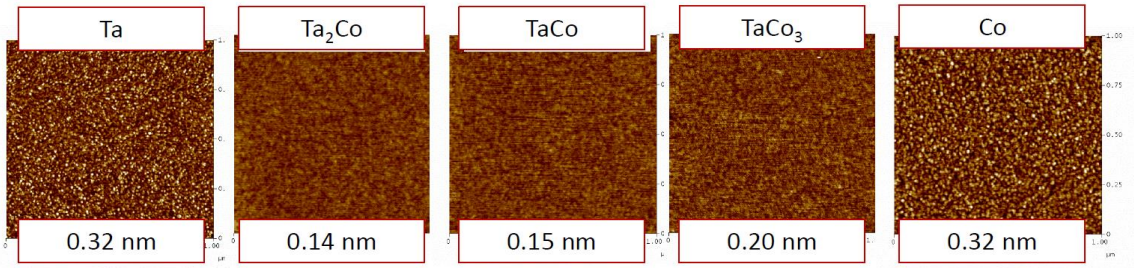

Fig. 9 AFM images of surface roughness with respective RMS values

3.1.5 Determination of optical constants

Next, the optical constants were experimentally determined by EUVR analysis as described in the experimental methods Sec. 2.1.3. Fig. 10 demonstrates the good agreement between the simulated and the measured data for the wavelength of 13.5 nm. The determined EUVR optical constants have been plotted and listed in Fig. 11.

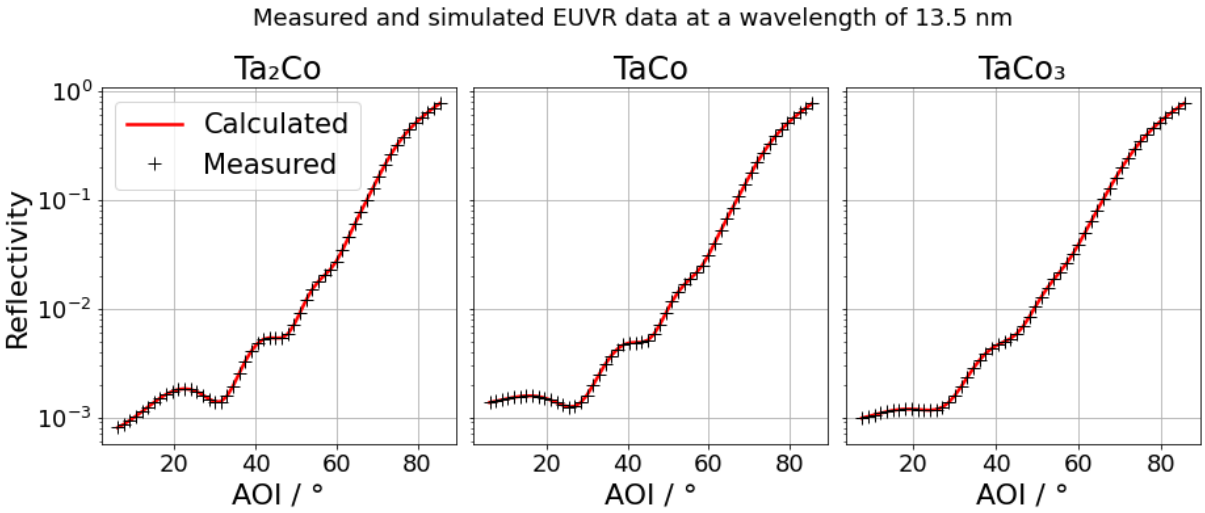

Fig. 10 The simulated reflectivity profiles regarding the best-fit values determined using the DE optimization, plotted against the measured data. The profiles were measured in the angular range from 6° to 85.5° (near normal)

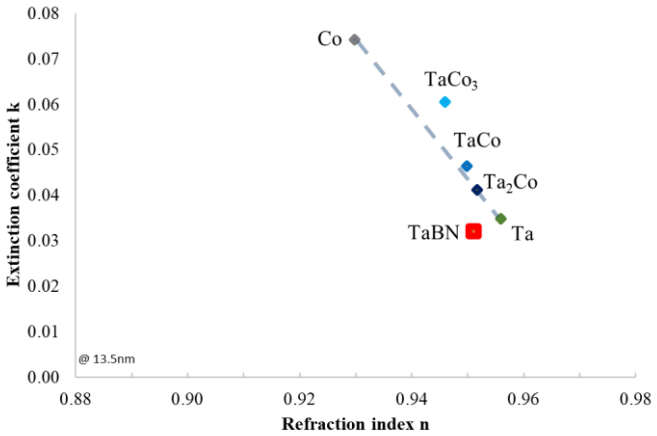

Material	n	k
Ta	0.95595	0.03481
Ta_2Co	0.95165	0.0411
TaCo	0.9498	0.0464
$TaCo_3$	0.94596	0.06051
Co	0.92984	0.07424

Fig. 11 Complex refractive index of Ta-Co alloys determined by EUVR analysis

The higher the Co concentration in the Ta-Co alloy, the lower the refractive index *n* and higher extinction coefficient *k*, as seen in Fig. 11. Experimentally determined optical properties of TaCo are almost on the linear trendline between those of Co and Ta and that of Ta_2Co is closer to the trendline (Fig. 11). However, the observed values of the optical constants for $TaCo_3$ deviate distinctively from the ideal linear trend highlighted by a grey dashed line (Fig. 11). A similar shift in optical properties for Ni-Al alloys was observed by Luong et al..[3] This shift was attributed to an oxidation-induced absorption edge shift. Ta does not have absorption edge energies close to the EUV wavelength of 13.5 nm. However, the M1 edge of Co lies at 101 eV,[46] which corresponds to ~12.3 nm, and is close to the EUV wavelength. In addition, an EDS scan revealed that, as the Ta-Co alloy's cobalt content increases, so does its O content in the bulk. Also, the deviation in optical constants increases with higher O and Co in the bulk, as we observe in Fig. 11. Thus, the fact that Co has an absorption edge close to the wavelength at which optical properties are determined, and oxygen has the ability to influence the absorption edge, the deviation in the optical properties of Ta-Co alloys from the linear trend line can be attributed to the oxidation induced absorption edge shift.

3.1.6 Durability in cleaning solutions

Fig. 12 shows the XRR analysis of Ta-Co alloys after treatment in different cleaning solutions compared to the pristine condition. Because the oscillation frequency remained constant, it may be concluded that TaCo and Ta_2Co compositions were stable in the cleaning solutions, and their thickness did not change after cleaning. The minor variations which distort curves from each other can be associated with surface effects like oxidation. On the other hand, the $TaCo_3$ samples that were treated with cleaning solutions exhibit thickness variation. AFM performed on all four $TaCo_3$ samples, summarized in Table 1, shows an increase in surface roughness after treatment.

The top layer of Co-rich oxide in $TaCo_3$ set it apart from the other two alloy compositions (cf. Sec. 3.1.3). Therefore, we included pure Co in the cleaning durability test and found it to be unstable in all cleaning solutions. XRR analysis revealed the entire thin layer to be damaged. Since even the critical angle has changed, we can conclude that there is no longer any Co on the substrate or only a trace amount of Co. This observation provides the reason why $TaCo_3$ failed the cleaning durability test.

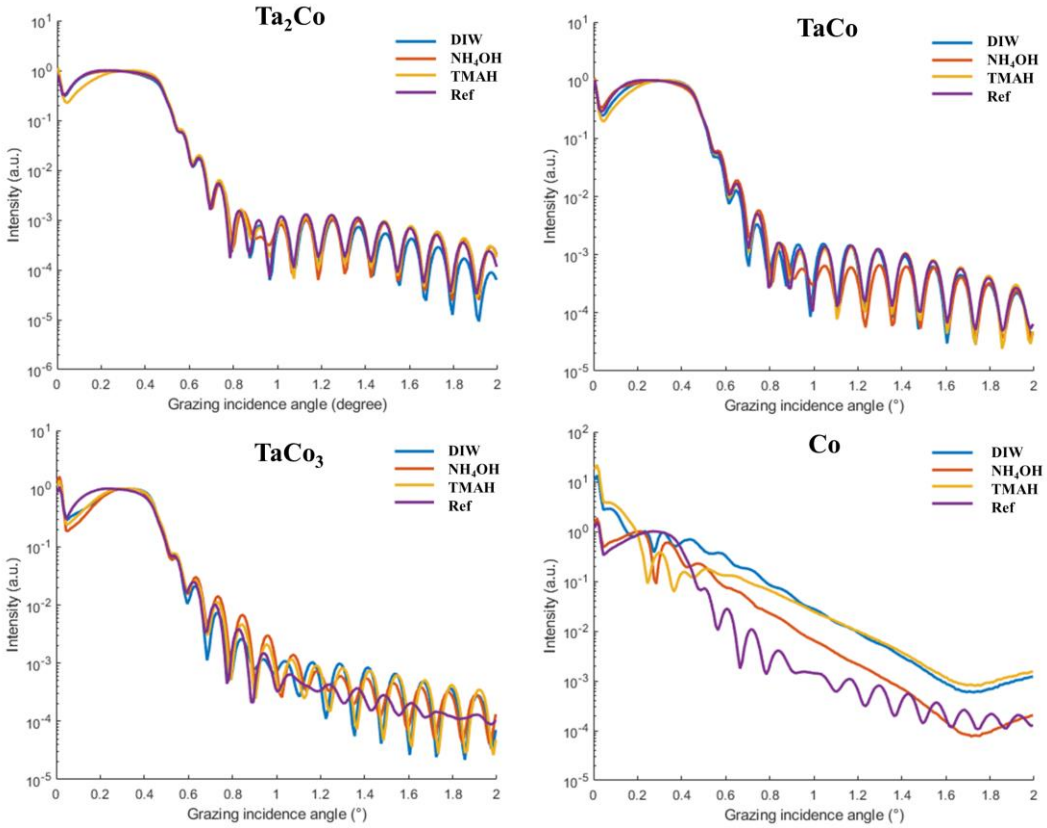

Fig. 12 XRR measurements of the beaker tests, the reference samples of the Ta-Co alloys, and Co

Table 1. Surface roughness of $TaCo_3$ samples by AFM after cleaning solutions treatment

Sample treatment	DIW	NH_4OH	TMAH	Reference
Surface roughness RMS (nm)	6.01	6.99	1.15	0.175

3.1.7 Stability in H-environment

Next, we test the stability of the Ta-Co alloys upon H_2 plasma exposure by RBS (Fig. 13). The amount of Ta and Co in the bulk composition of these materials is stable in H_2 plasma, with no significant difference in elemental content before and after exposure. There were no visible blisters on the surfaces of these samples, indicating that no damage had occurred. This finding is consistent with the conclusions of Stortelder et al.,[8] who found that TaCo alloy was resistant to hydrogen plasma.

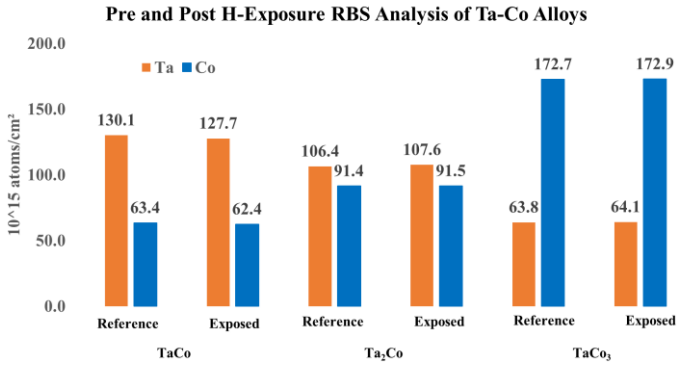

Fig. 13 RBS analysis of the as-deposited Ta-Co alloys and after exposure to H radicals for 24 hrs. The vertical bars indicate the areal density of Ta and Co in atoms per square cm present in the thin film.

3.1.8 Long-term stability assessment

Fig. 14 depicts the progression of the film's oxide thickness over a period of about one year following the deposition, from pure Ta over the three Ta-Co alloys to pure Co. During the initial weeks, all samples exhibit a rapid increase in the oxide thickness. The oxide thickness of the Ta film appears to have remained constant throughout the period. Ta_2Co and TaCo samples show a gradual increment in oxide thickness. Whereas Co-rich samples demonstrate a strong and steady degradation. Even after a year, Ta-Co films with high Co content developed a surface oxide thickness of more than 4 nm, which seems to keep growing linearly and stronger than on the Ta-rich compounds. Pure Co and $TaCo_3$ composition exhibit rapid growth in the oxide layer, and an oxide thickness of almost 10 nm was determined for both samples. Even while the growth appears to be slowing down with time, it is still significant. As mentioned previously (cf. Sec. 3.1.6), the unstable Co-rich oxide is responsible for the $TaCo_3$ degradation. Therefore, Co films or $TaCo_3$ cannot be employed as an alternate absorber layer because of their rapid and continuous growth of the surface oxide, which continuously alters its optical performance over time.

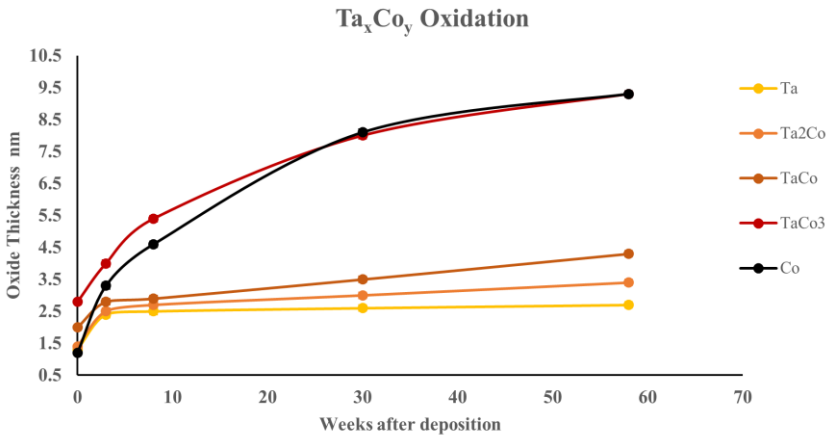

Fig. 14 Stability of Ta-Co alloys over time. The figure highlights the change in the oxide thickness of each sample over a period of weeks after deposition. The obtained oxide thickness has been extracted from the XRR measurements.

3.1.9 Automated cleaning assessment on a commercial tool

After the preliminary cleaning investigation that involved beaker tests, the TaCo composition was selected for a more detailed characterization. This involved automated cleaning inside the "Mask Track Pro" cleaning tool, of a full 300 mm silicon wafer deposited with 30 nm TaCo alloy thin film. The automated cleaning recipe used strong oxidative chemistry followed by a mega-sonic cleaning in alkaline conditions. The XRR and AFM measurements have been summarized in Fig. 15 and Table 2. Considering the results obtained from TEM and EDS-STEM analysis (Sec. 3.1.3), a simple two-layer model consisting of a Ta-rich surface oxide and TaCo bulk composition was utilized for the XRR curve fitting. The XRR measurements indicate no significant damage to TaCo coated wafer after undergoing a number of cleaning cycles. Although, a detailed observation of XRR results shows a slight reduction in the oxide layer thickness and smoothening of the surface. The AFM measured the surface roughness over an area of 2x2 µm², and these results contradict the trend observed in the surface roughness of XRR results. The surface roughness data assessed by these two approaches typically are not likely to be consistent since each tool covers distinct ranges of lateral spatial frequency, as well as because of the nature of the probing depth.[53] Literature has suggested using these two surface roughness determination approaches complementary to each other.

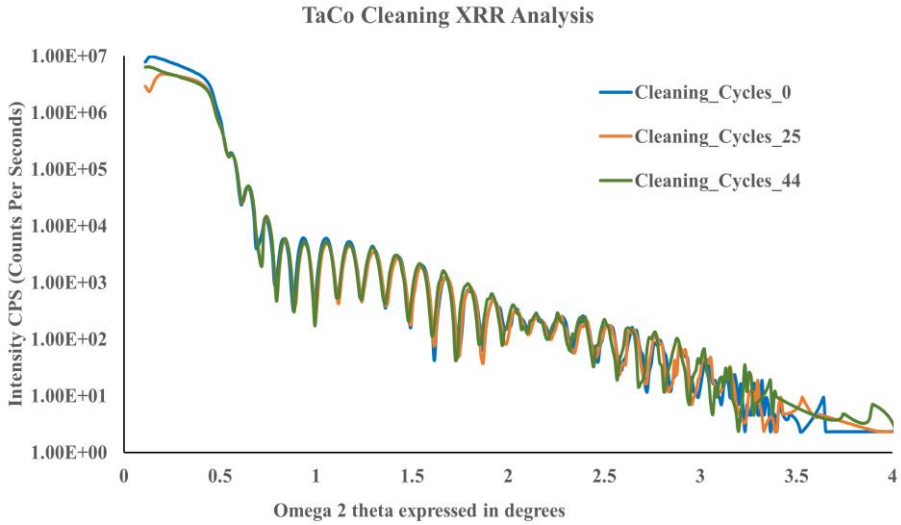

Fig. 15 TaCo thin films were subjected to XRR measurements following the indicated cleaning cycles.

Table 2. AFM surface roughness measurements and estimated surface roughness, surface oxide thickness, and bulk thickness of TaCo thin film from XRR curve fitting. The values mentioned between brackets indicate the error in calculation by the vendor's (Bruker) software and the errors due to error propagation.

Cleaning Cycles	Surface Roughness RMS (nm) AFM	Surface Roughness (nm) XRR	Ta Rich surface Oxide Thickness (nm)	TaCo Thickness (nm)	Total Film Thickness (nm)
0	0.04	0.30 (± 0.01)	3.18 (± 0.02)	28.53 (± 0.02)	31.71 (± 0.04)
25	0.1	0.48 (± 0.01)	3.09 (± 0.02)	28.73 (± 0.02)	31.81 (± 0.04)
44	0.15	0.41 (± 0.01)	3.06 (± 0.01)	29.06 (± 0.02)	32.12 (± 0.03)

3.1.10 Etch results

In this subsection, we will go over the findings of the ICP etch study that was conducted to understand the etch mechanism and etch selectivity of TaCo over Ru, as well as to assess the suitability of prospective hard mask materials such as SiO_2 and Si_3N_4. Fig. 16 shows results from Cl_2/Ar etch recipe as described earlier. The etch depth versus time was evaluated with 10W RIE power to verify the linearity of the TaCo etch rate (cf. Fig. 16(a)). Etch rates were then evaluated versus RIE power (at 0, 10, and 20 W) (cf. Fig. 16(b)). The data for Ta is not shown since the 50 nm Ta film was entirely removed within 5 minutes at 10 W RIE, indicating a significantly higher etch rate than TaCo or Ru. At 0 W RIE, etch rates were very low, showing that the chemical etching did not play a role; therefore, this would not offer a route to selective etching. At 10 W or 20 W RIE, the etch selectivity of TaCo to Ru was ≥4, which suggests that this process may be a candidate for TaCo patterning, especially if combined with an endpoint detector to enable accurate detection and etch stop on the underlying Ru layer. However, the etch selectivity of TaCo to the proposed SiO_2 or Si_3N_4 hard mask materials was low, indicating that an alternative hard mask would be required. The etch mechanism shows the characteristics of an ion-assisted etch, with Ta etching easily in the chlorine chemistry, but Co requires a more physical component. Overall, an acceptable TaCo:Ru selectivity was achieved even though the ion beam sputter rate and sputter yield of Co and Ru in Ar ion bombardment are similar.[54][55]

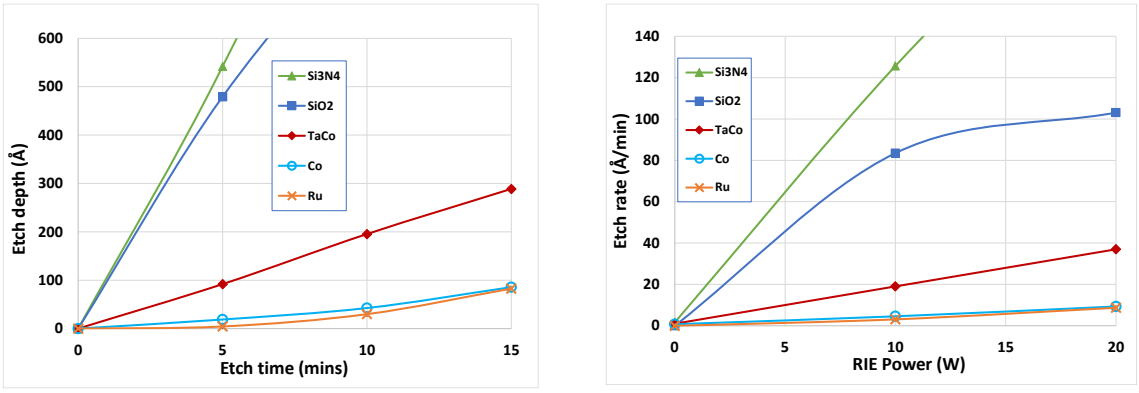

(a) (b)

Fig. 16 Etch depth (a) versus etch time using 10W RIE power and etch rate (b) versus RIE power via ICP for various layers using Cl_2/Ar.

3.1.11 Experimental results summary

Table 3 summarizes the highlights obtained from the experimental analysis of Ta-Co alloys. It can be observed that Ta-Co alloys are homogeneous and amorphous in nature. The composition of an alloy strongly influences the surface oxide and roughness. Ta-Co alloy compositions have a lower refractive index *n* and a greater EUV extinction coefficient *k* than the currently used Ta-based absorber. All compositions under consideration were stable in the H environment. Only TaCo and Ta_2Co were stable in the cleaning solutions and demonstrated moderate surface oxide stability over a long period. Therefore, from the standpoint of their material properties, TaCo and Ta_2Co are suitable candidates as EUV mask absorbers. The TaCo alloy etch experiments also confirmed a good etch selectivity with respect to the Ru layer and recommend seeking better candidates for the hard mask.

Table 3. Ta-Co Alloys experimental evaluation summary

Evaluation	Ta_2Co	TaCo	$TaCo_3$
Film properties Uniformity Composition Ta:Co Density (XRR) Phase	 Homogenous 0.67:0.33 14.3 g/cm^3 Amorphous	 Homogenous 0.54:0.46 14.9 g/cm^3 Amorphous	 Homogenous 0.27:0.73 12.1 g/cm^3 Amorphous
Top layer thickness and composition Roughness (AFM-RMS)	3 nm Ta-rich oxide 0.15 nm	3 nm Ta-rich oxide 0.14 nm	2 nm Co-rich oxide 0.20 nm
Optical constants n k	 0.95165 0.0411	 0.9498 0.0464	 0.94596 0.06051
Stability in cleaning solutions	Stable	Stable	Unstable
H_2 plasma test	Stable thickness and composition No blisters	Stable thickness and composition No blisters	Stable thickness and composition No blisters
Oxide stability over time	Moderately Stable	Moderately Stable	Unstable
Etch selectivity TaCo:Ru	-------	≥4	-------

3.2 Simulation Results

In this section, we compare the imaging performance of the selected thickness of Ta-Co alloy absorbers with the current Ta-based absorber having a thickness of 60 nm. The absorber thickness of Ta-Co alloys and Ta-based absorber with corresponding simulated EUV reflectivity and phase shift at 5.355 deg CRAO are listed in Table 4. The absorber EUV reflectivity is determined by considering an absorber stack placed on the ML mirror stack. Phase shift is the difference in phase between light that only travels through the ML mirror and light that travels through the ML mirror plus absorber, calculated at the absorber height. The higher the Co concentration in the Ta-Co alloy, the lower is the reflectivity and the larger is the phase shift, in accordance with the optical properties. It is important to keep in mind that these values are specific to the selected absorber thickness.

Table 4. Proposed Ta-Co alloy thickness with corresponding reflectivity and phase shift

Composition	Absorber thickness (nm)	Reflectivity (%)	Phase Shift (°)
Ta_2Co	52	0.56	141.70
TaCo	52	0.24	151.84
$TaCo_3$	51	0.23	202.31
Ta-based	60	1.29	156.28

Next, we discuss in detail the imaging performance of Ta-Co alloy absorbers for two types of patterns, viz. LnS and CH, as mentioned in Sec. 1.2 (simulation methods)

3.2.1 line and space imaging performance

A comparison of the through-pitch imaging performance of Ta-Co alloys with a Ta-based absorber for horizontal LnS pattern targeting 10 nm wafer CD and using the leaf-shape dipole illumination (cf. Fig. 3(a)) is displayed in Fig. 17. All Ta-Co alloy compositions exhibit improved NILS, as shown in Fig. 17 (a). As observed in the experimental results, the higher the Co concentration in the Ta-Co alloy, the lower the refractive index *n* and the higher the extinction coefficient *k*; this trend leads to an improved NILS, as anticipated.

In Fig. 17 (b), we can observe a reduction in best focus variation through pitch for all Ta-Co alloy compositions compared to the reference Ta-based absorber. This phenomenon is attributed to the fact that Ta-Co alloys have greater *k* values than Ta-based absorbers. This finding confirms that higher *k* values reduce best focus variation through pitch, as anticipated by Philipsen et al..[5]

Fig. 17(c) shows increased TCE for Ta-Co alloys compared to the reference Ta-based absorber. As mentioned earlier, we set the upper limit of TCE for the smallest pitch to 10 mrad, which has been approached. TCE for a larger pitch is still below the recommended value of 20 mrad.

It can be observed in Fig. 17(d) that Ta-Co alloy absorber masks require a lower TtS value compared to the Ta-based absorber mask, as expected. High-*k* materials are meant to have lower EUV reflectivity at a similar thickness and, therefore, a reduction in TtS. This can also be verified with absorber reflectivity values listed in Table 4.

From Fig. 17(e), it is clear that Ta-Co alloy absorber masks exhibit no significant difference in throughput criterion compared to a Ta-based absorber mask, even at lower absorber thickness which can be considered as an advantage. The mask bias used for each pitch to print on target is indicated in Fig. 17(f). The mask bias is calculated as (mask CD–target CD). The mask bias is optimized to obtain the highest NILS at the smallest pitch. The effect of mask bias on the other imaging metrics is discussed later in this paper (see Sec. 3.2.4).

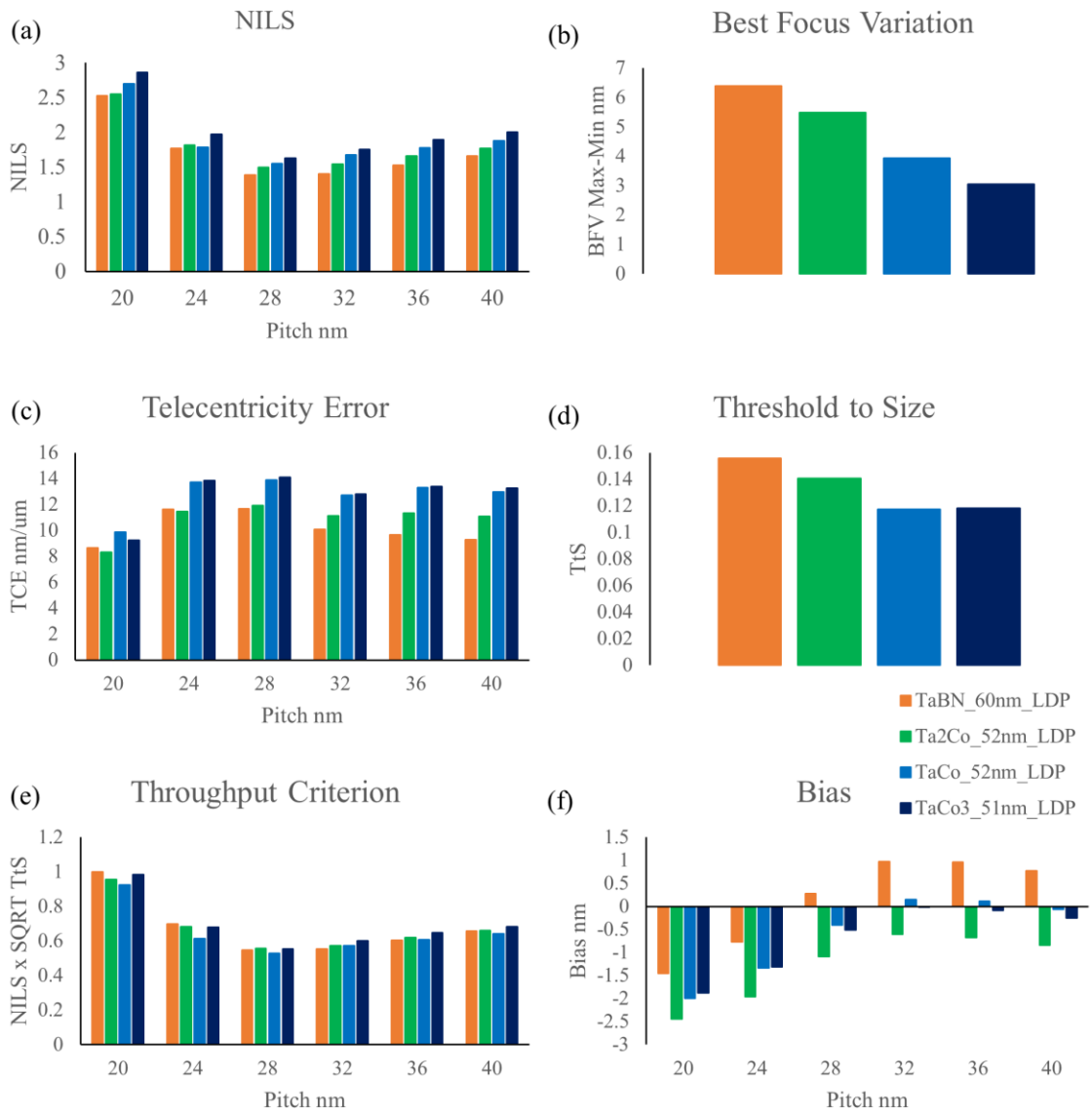

Fig. 17 Comparison of the Through-pitch imaging performance of Ta-Co alloy masks with a Ta-based absorber mask for horizontal LnS pattern (a) NILS, (b) best focus variation through pitch, (c) telecentricity error, (d) threshold to size, (e) throughput criterion, (f) mask bias.

A similar comparison of the through-pitch imaging performance of Ta-Co alloy absorber masks with a Ta-based absorber mask for vertical LnS pattern using the leaf-shape dipole illumination (cf. Fig. 3(b)) is shown in Fig. 18. Almost identical observations can be found for all imaging metrics under consideration. Improved NILS with lower BFV appears to be an advantage (Fig. 18(a)&(b)). Although TtS for Ta-Co alloys is reduced, it is compensated by a throughput criterion that is comparable to a reference Ta-based absorber (Fig. 18(c)&(d)).

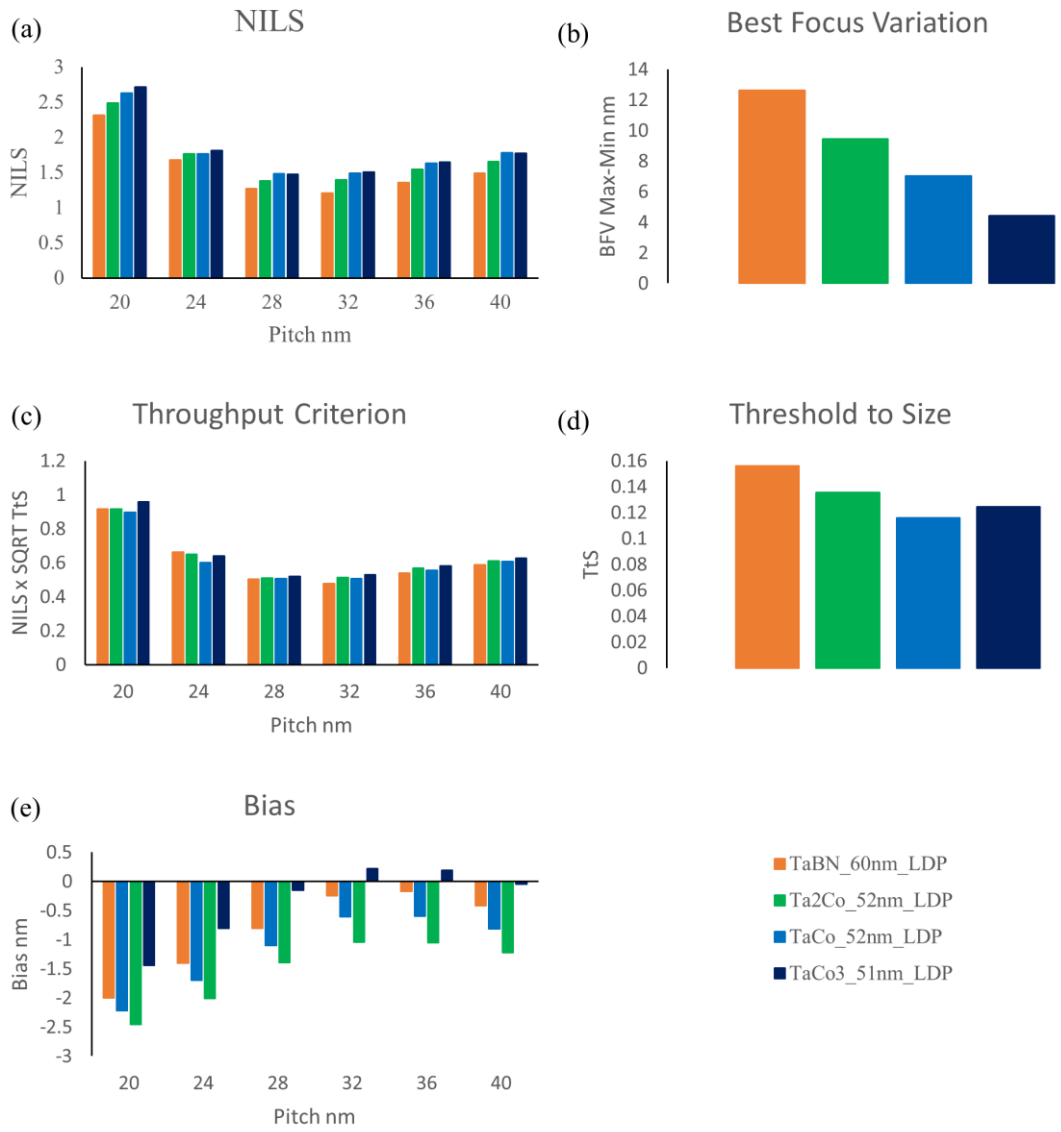

Fig. 18 Comparison of the Through-pitch imaging performance of Ta-Co alloy absorber masks with a Ta-based absorber mask for vertical LnS pattern (a) NILS, (b) best focus variation through pitch, (c) threshold to size, (d) throughput criterion, (e) mask bias.

3.2.3 Square contact hole array imaging

Fig. 19 shows a comparison of the through-pitch imaging performance of Ta-Co alloy absorber masks with a Ta-based absorber mask for the CH pattern in a square array using the leaf-shaped quasar (cf. Fig. 3(c)). The imaging metrics are evaluated along the horizontal cutline through the center of the square contact hole. For all imaging metrics under evaluation, observations similar to the LnS pattern can be identified for contact holes. Improved NILS combined with a reduced BFV tends to be favorable (Fig. 19(a)&(b)). In comparison to Ta-based absorber, the TCE of Ta-Co alloy absorbers is higher for the smallest pitch, that is within the set limit of 10 mrad, but there is no clear trend for larger pitch (Fig. 19(c)). Comparing Fig. 19(d) with Fig. 17(d) & Fig. 18(d), the TtS values of contact hole patterns with Ta-Co alloy absorbers appear to be considerably lower than that of the reference Ta-based absorber in comparison to the LnS pattern case, which can be attributed to mask bias impact. This low TtS also reduces the throughput criterion for Ta-Co alloys (Fig. 19(e)).

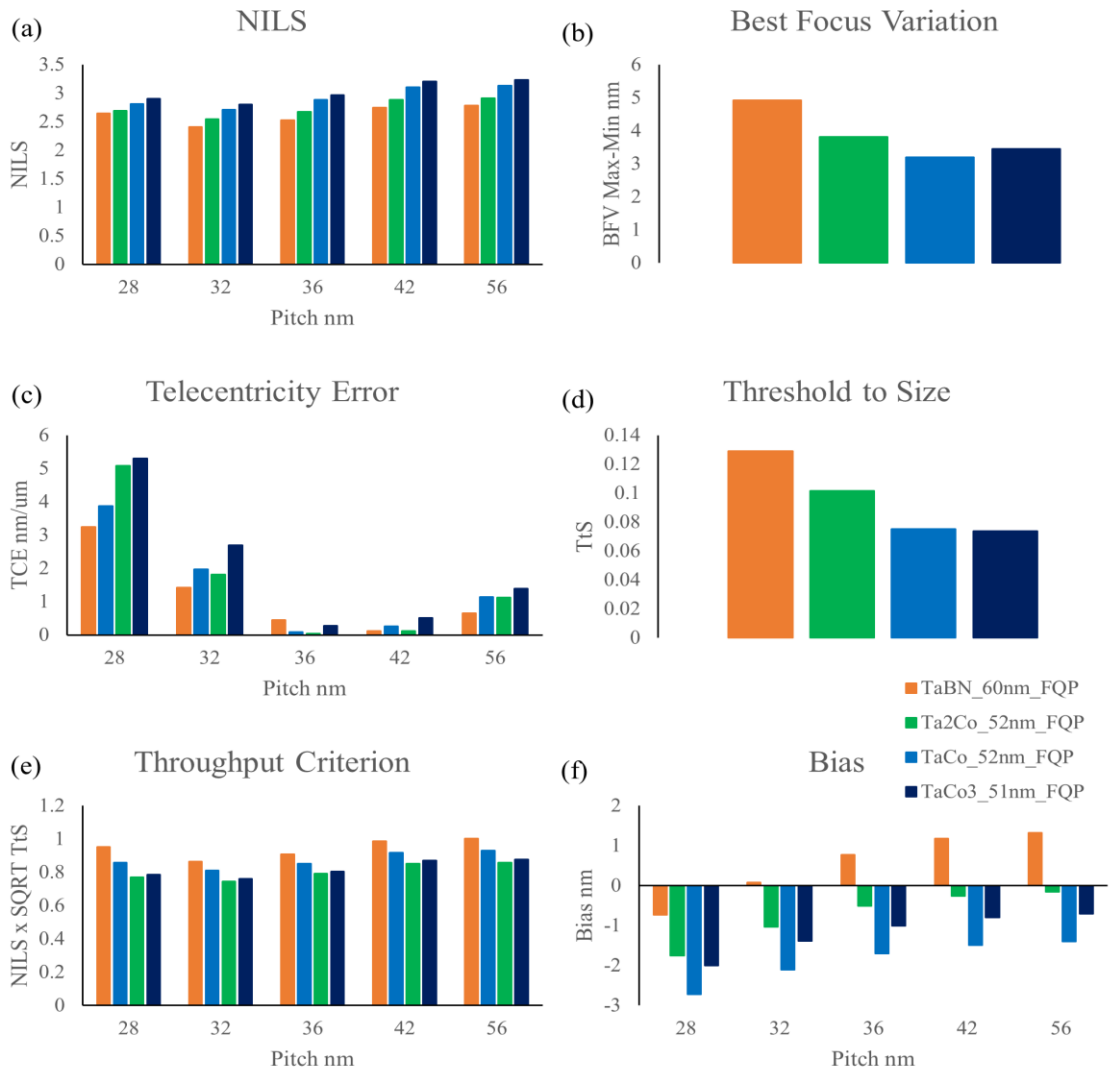

Fig. 19 Comparison of the Through-pitch imaging performance of Ta-Co alloy absorber masks with a Ta-based absorber mask for square array CH patterns (a) NILS, (b) best focus variation through pitch, (c) telecentricity error, (d) threshold to size, (e) throughput criterion, (f) mask bias.

3.2.4 Understanding the impact of mask bias on imaging metrics

In this sub-section, we intend to understand the impact of mask bias on NILS, TCE, and TtS. We employ a 52 nm TaCo alloy absorber as a case study for this part of the simulation. The TtS values that can print a wafer-level target of a 10 nm trench with a 20 nm pitch for a horizontal LnS pattern using the full leaf-shape dipole illumination (Fig. 3 (a)) have been reported in Fig. 20 (c). NILS and TCE have been evaluated at this particular threshold in a similar way as described in the methodology section (Sec. 2.2) and plotted as a function of focus for different mask biases in Fig. 20 (a) and (b), respectively. A negative mask bias indicates that the actual trench on the mask is smaller than the intended target, whereas a positive mask bias indicates the converse. NILS increases with a negative mask bias, reaches a maximum at -2 nm mask bias, and decreases again (Fig. 20 (a)). TCE, on the other hand, shows a reversed trend, decreasing with a positive mask bias and approaching zero at +3/+4 nm mask bias (Fig. 20 (b)). Since we have chosen the mask bias that results in maximum NILS, TCE turns out to be less than optimal. However, NILS would have been compromised if the emphasis had been set on minimizing TCE. A wider trench indicates larger exposure of the ML

mirror, and with increased ML reflectivity, we observe an increment in TtS as expected (Fig. 20 (c)). We can also observe that the TtS is almost independent of focus variation for each bias value.

Since we are using a full leaf shape dipole in which point sources are distributed symmetrically around the telecentric sigma, the best focus (focus value corresponding to max NILS) exhibits no variation, which is also evident from the NILS plot. These findings apply only to the LDP illumination source and may differ for other illumination sources and absorber materials.

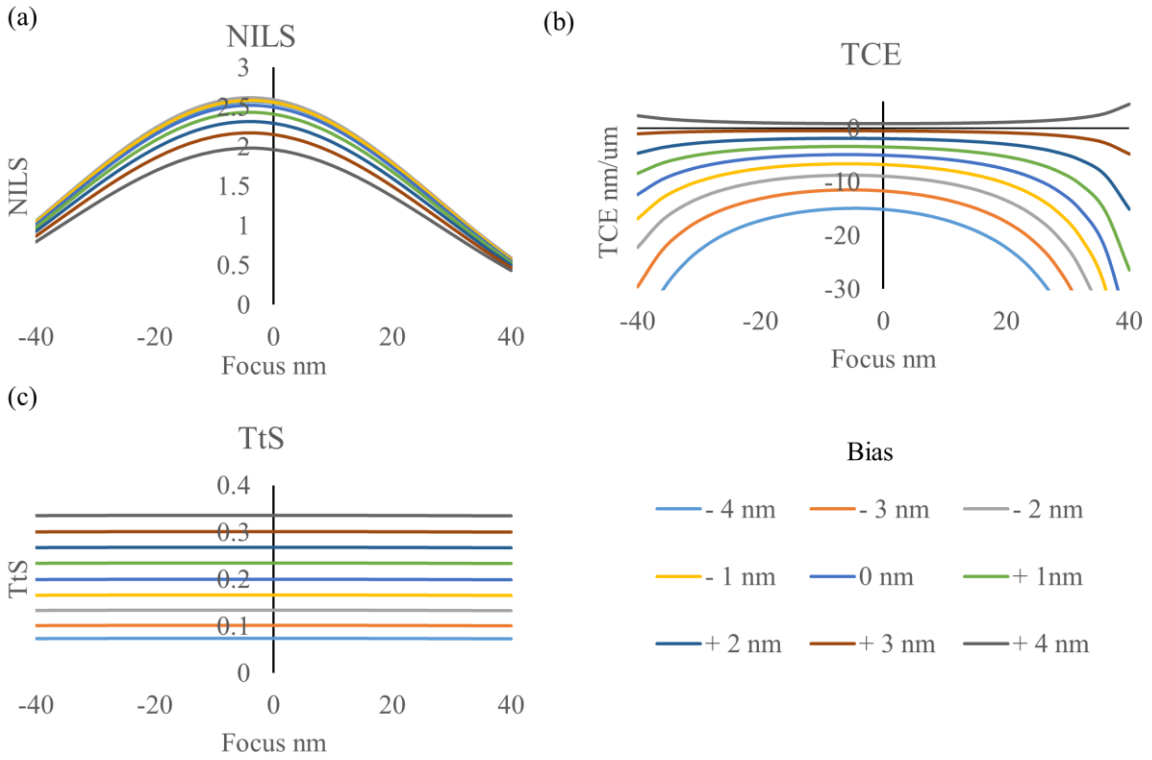

Fig. 20 Impact of mask bias on imaging metrics as a function of focus (a) NILS, (b)TCE, and (c) TtS of a 52 nm TaCo alloy absorber mask using LDP illumination source. The wafer level target is a 10 nm trench with a 20 nm pitch for a horizontal LnS pattern.

3.2.5 Simulation results summary

In summary, the simulation results of Ta-Co alloys as a novel EUV absorber mask for the patterns considered in this study targeting NA 0.55 show consistency in NILS improvement and BFV reduction compared to the Ta-based mask due to their higher EUV extinction coefficient. The mask bias was established through NILS optimization. The selected thickness of Ta-Co alloys and mask bias show increased TCE for the smallest pitch in comparison to the reference Ta-based absorber. Although horizontal LnS patterns with larger pitch exhibit increased TCE, they are still below the recommended values. The selected mask bias to print on target has a huge impact on the imaging metrics. A further topic not covered in this work is the effect of illumination source shapes on imaging metrics, which will be followed in our subsequent study.

4 Conclusions

Ta-Co alloys have confirmed a lower refractive index *n* and a higher EUV extinction coefficient *k* than the current industry standard Ta-based absorber. The oxidation-induced absorption edge shift is responsible for the optical characteristics of Ta-Co alloys deviating from the linear trend line, and this deviation increases with higher O and Co in the bulk. From experimental analyses, it is evident that TaCo and Ta_2Co can withstand an aggressive hydrogen environment and mask-cleaning conditions. In contrast, $TaCo_3$ cannot withstand mask cleaning conditions due to Co segregation and an unstable oxide layer. $TaCo_3$ also failed the long-term stability assessment. Therefore, the $TaCo_3$ composition is considered unsuitable as a novel absorber candidate, even though its imaging performance in terms of NILS is better as compared to the other Ta-Co alloy compositions. The qualifying compositions, namely TaCo and Ta_2Co, show a reduction in M3D effects at lower absorber thickness compared to the reference Ta-based absorber of 60 nm; in particular, improved NILS and reduced BFV, all of which are attributed to the optical properties of those materials. No advantage is observed in terms of TCE and TtS. Ignoring the reduction in TtS, the qualifying Ta-Co compositions exhibit a clear advantage in the instance where only vertical LnS patterns are required. Similarly, the advantages for dark field CH imaging appear to be reasonable. It is important to note that these imaging metrics vary depending on the mask bias. Also, the illumination source shape impacts the M3D metrics and can be tuned to minimize TCE for horizontal LnS patterns. Therefore, Source Mask Optimization (SMO) aiming at co-optimizing multiple metrics for any design is a recommended next step in the feasibility study and towards implementation of novel absorber masks. In a subsequent article, we will address the trade-offs in EUV imaging metrics for Ta-Co alloys as a function of absorber thickness and illumination source shapes. Furthermore, the results from the etch study indicate that an etch selectivity of ≥4 could be obtained for TaCo versus Ru. To enable accurate detection and etch stop on the underlying Ru layer, patterning of TaCo alloy absorber in combination with an end point detector is suggested. Since the TaCo selectivity to the proposed SiO_2 and Si_3N_4 hard mask materials was unfortunately low, different hard mask materials will require further exploration.

Acknowledgments

The authors acknowledge that this project has received funding from the Electronic Component Systems for European Leadership Joint Undertaking under grant agreement No 783247 - TAPES3 (Technology Advances for Pilot line of Enhanced Semiconductors for 3 nm). This Joint Undertaking receives support from the European Union's Horizon 2020 research and innovation program alongside the Netherlands, Belgium, Germany, France, Austria, United Kingdom, Israel, and Switzerland. The authors would like to thank the Materials and Component Analysis (MCA) department at imec for material characterizations and Ivan Pollentier (imec) for hydrogen stability experiments. Finally, we thank Synopsys for supporting us with the S-Litho EUV simulation tool.

References

[1] C. C. Dunbar, "Redefining innovation during The Renaissance of Computing," in Photomask Technology 2021, S. P. Renwick, Ed., SPIE (2021). https://doi.org/10.1117/12.2605755

[2] A. Erdmann et al., "Characterization and mitigation of 3D mask effects in extreme ultraviolet lithography," Adv. Opt. Technol. 6(3–4) (2017) . https://doi.org/10.1515/aot-2017-0019

[3] V. Vu et al., “Christian Laubis, Frank Scholze, and Marc Heyns,” Ni-Al Alloys as Alternative EUV Mask Absorber 8 (2018). https://doi.org/10.3390/app8040521
[4] A. Erdmann et al., "Perspectives and tradeoffs of absorber materials for high NA EUV lithography," J. Micro. Nanolithogr. MEMS MOEMS 19(04) (2020). https://doi.org/10.1117/1.JMM.19.4.041001
[5] C. Detavernier et al., "Novel EUV mask absorber evaluation in support of next-generation EUV imaging," in Photomask Technology 2018, J. H. Rankin and E. E. Gallagher, Eds., SPIE (2018). https://doi.org/10.1117/12.2501799
[6] M. Wu et al., "Mask absorber for next generation EUV lithography," in Extreme Ultraviolet Lithography 2020, K. G. Ronse et al., Eds., SPIE (2020).https://doi.org/10.1117/12.2572114
[7] V. Philipsen et al., "Reducing extreme ultraviolet mask three-dimensional effects by alternative metal absorbers," J. Micro. Nanolithogr. MEMS MOEMS 16(4), 041002 (2017) https://doi.org/10.1117/1.JMM.16.4.041002
[8] J. Stortelder et al., "First results of EUV-scanner compatibility tests performed on novel 'high-NA' reticle absorber materials," in International Conference on Extreme Ultraviolet Lithography 2021, K. G. Ronse et al., Eds., SPIE (2021).https://doi.org/10.1117/12.2600928
[9] P. Wang et al., "Thermodynamic assessment of the Co-Ta system," CALPHAD 64, 205–212 (2019) https://doi.org/10.1016/j.calphad.2018.12.002
[10] H. M. S. Mesilhy et al., "Pathfinding the perfect EUV mask: the role of the multilayer," in Extreme Ultraviolet (EUV) Lithography XI, N. M. Felix and A. Lio, Eds., SPIE (2020). https://doi.org/10.1117/12.2551870
[11] J. K.-C. Chen et al., "Directional etch of magnetic and noble metals. I. Role of surface oxidation states," J. Vac. Sci. Technol. A 35(5), 05C304 (2017) https://doi.org/10.1116/1.4983829
[12] J. K.-C. Chen et al., "Directional etch of magnetic and noble metals. II. Organic chemical vapor etch," J. Vac. Sci. Technol. A 35(5), 05C305 (2017)https://doi.org/10.1116/1.4983830
[13] N. D. Altieri et al., "Review Article: Plasma–surface interactions at the atomic scale for patterning metals," J. Vac. Sci. Technol. A 35(5), 05C203 (2017) https://doi.org/10.1116/1.4993602
[14] V. Luong et al., "Assessing stability of metal tellurides as alternative photomask materials for extreme ultraviolet lithography," J. Vac. Sci. Technol. B Nanotechnol. Microelectron. 37(6), 061607 (2019) https://doi.org/10.1116/1.5125662
[15] J. K.-C. Chen et al., "Ion beam assisted organic chemical vapor etch of magnetic thin films," J. Vac. Sci. Technol. A 35(3), 031304 (2017) https://doi.org/10.1116/1.4978553
[16] B. Henke, E. Gullikson, and J. Davis, "X-ray interactions: Photoabsorption, scattering, transmission, and reflection at E = 50-30,000 eV, Z = 1-92. Atomic Data Nucl. Data Tables," 181–342 (1993). https://doi.org/10.1006/adnd.1993.1013
[17] Chao, Julie (2013-06-24). "Development of new advanced materials to get boost - Berkeley Lab," News Center, 24 June 2013, <https://newscenter.lbl.gov/2013/06/24/development-of-new-advanced-materials-to-get-boost/> (accessed 1 February 2023).
[18] A. Jain et al., "Commentary: The Materials Project: A materials genome approach to accelerating materials innovation," APL Mater. 1(1), 011002 (2013) https://doi.org/10.1063/1.4812323 [https://materialsproject.org/#apps/phasediagram]
[19] G. Brandt et al., "The Metrology Light Source – The new dedicated electron storage ring of PTB," Nucl. Instrum. Methods Phys. Res. B 258(2), 445–452 (2007) https://doi.org/10.1016/j.nimb.2007.02.076

[20] Price, K., Storn, R. and Lampinen, J., *Differential Evolution: A Practical Approach to Global Optimization*, p. 463-477, Springer (December 22, 2005)
[21] P. Virtanen et al., “van Mulbregt, and SciPy 1.0 Contributors, "SciPy 1.0: fundamental algorithms for scientific computing in Python,” Nature Methods 17, 261–272 (2020).
[22] D. L. Windt et al., "Optical constants for thin films of C, diamond, Al, Si, and CVD SiC from 24 Å to 1216 Å," Appl. Opt. 27(2), 279 (1988) https://doi.org/10.1364/ao.27.000279
[23] B.L. Henke, E.M. Gullikson, and J.C. Davis, "X-ray interactions: photoabsorption, scattering, transmission, and reflection at E=50-30000 eV, Z=1-92," Atomic Data and Nuclear Data Tables Vol. 54 (no.2), 181-342 (July 1993). https://doi.org/10.1006/adnd.1993
[24] A. Andrle et al., "The anisotropy in the optical constants of quartz crystals for soft X-rays," J. Appl. Crystallogr. 54(2), 402–408 (2021) https://doi.org/10.1107/s1600576720016325
[25] L. Parratt, “Surface studies of solids by total reflection of X-Rays,” Phys. Rev. 95(2), 359–369 (1954).
[26] L. Névot and P. Croce, “*Caractérisation des surfaces par réflexion rasante de rayons X. Application à l’étude du polissage de quelques verres silicates*,” Rev. Phys. Appl. 15(3), 761–779 (1980).
[27] L. L. Cheong et al., "EUV mask cleans comparison of frontside and dual-sided concurrent cleaning," in Extreme Ultraviolet (EUV) Lithography VI, O. R. Wood and E. M. Panning, Eds., SPIE (2015). https://doi.org/10.1117/12.2085913
[28] A. Mark et al., "EUV-induced hydrogen plasma: pulsed mode operation and confinement in scanner," J. Micro/Nanopattern. Mats. Metro 20(3) (2021). https://doi.org/10.1117/1.JMM.20.3.033801
[29] [21] J. Meersschaut et al., "CNT EUV pellicle: moving towards a full-size solution," in Photomask Technology, E. E. Gallagher and P. D. Buck, Eds., SPIE (2017). https://doi.org/10.1117/12.2280632
[30] EUV Tech Hydrogen Cleaner (Apparatus) https://pereravineyard.com/hydrogen-cleaner
[31] E. van Setten et al., "Edge placement error control and Mask3D effects in High-NA anamorphic EUV lithography," in International Conference on Extreme Ultraviolet Lithography 2017, P. A. Gargini et al., Eds., SPIE (2017). https://doi.org/10.1117/12.2280624
[32] I. A. Makhotkin et al., "Refined extreme ultraviolet mask stack model," J. Opt. Soc. Am. A Opt. Image Sci. Vis. 38(4), 498 (2021)https://doi.org/10.1364/josaa.416235
[33] J. Van Schoot et al., "High-NA EUV lithography exposure tool: advantages and program progress," in Extreme Ultraviolet Lithography 2020, K. G. Ronse et al., Eds., SPIE (2021). https://doi.org/10.1117/12.2572932
[34] B. Bilski et al., "High-NA EUV imaging: challenges, status and outlook" Photo Mask Japan April 2021
[35] J.-H. Franke et al., "Improving exposure latitudes and aligning best focus through pitch by curing M3D phase effects with controlled aberrations," in International Conference on Extreme Ultraviolet Lithography 2019, K. G. Ronse et al., Eds., SPIE (2019). https://doi.org/10.1117/12.2537104
[36] M. Burkhardt, "Investigation of alternate mask absorbers in EUV lithography," in Extreme Ultraviolet (EUV) Lithography VIII, E. M. Panning and K. A. Goldberg, Eds., SPIE (2017). https://doi.org/10.1117/12.2258266

[37] M. S. Hazem et al., "Pathfinding the perfect EUV mask: understanding the EUV mask using the hybrid mask model," in Proc. SPIE 11854, International Conference on Extreme Ultraviolet Lithography 2021, 118540U (2021). https://doi.org/10.1117/12.2601243
[38] D. Thakare, A. Delabie, and V. Philipsen, "Optimizing EUV imaging metrics as a function of absorber thickness and illumination source: simulation case study of Ta-Co alloy," in 37th European Mask and Lithography Conference, U. Behringer, Ed., SPIE (2022). https://doi.org/10.1117/12.2640098
[39] N. V. Davydova et al., "Fundamental understanding and experimental verification of bright versus dark field imaging," in Extreme Ultraviolet Lithography 2020, K. G. Ronse et al., Eds., SPIE (2020). https://doi.org/10.1117/12.2573161
[40] Y. Chen et al., "Tip-to-tip variation mitigation in extreme ultraviolet lithography for 7 nm and beyond metallization layers and design rule analysis," J. Vac. Sci. Technol. B Nanotechnol. Microelectron. 35(6), 06G601 (2017) https://doi.org/10.1116/1.4994908
[41] C. Zahlten et al., "High-NA EUV lithography: pushing the limits," in 35th European Mask and Lithography Conference (EMLC 2019), U. F. Behringer and J. Finders, Eds., SPIE (2019). https://doi.org/10.1117/12.2536469
[42] J. Van Schoot et al., "High-NA EUV lithography exposure tool: program progress," in Extreme Ultraviolet (EUV) Lithography XI, N. M. Felix and A. Lio, Eds., SPIE (2020). https://doi.org/10.1117/12.2551491
[43] K. P. Gupta, "The co-Cr-ta (cobalt-chromium-tantalum) system," J. Phase Equilibria Diffus. 26(1), 93–97 (2005) https://doi.org/10.1007/s11669-005-0072-x
[44] C. S. Petersson et al., "Silicides of ruthenium and osmium: Thin film reactions, diffusion, nucleation, and stability," J. Appl. Phys. 53(7), 4866–4883 (1982) https://doi.org/10.1063/1.331319
[45] jcpds: 00-015-0806
[46] jcpds: 00-050-1337
[47] jcpds: 00-038-1449
[48] C. Lavoie et al., "Effects of alloying elements on cobalt silicide formation," J. Electron. Mater. 31(6), 597–609 (2002) https://doi.org/10.1007/s11664-002-0131-6
[49] jcpds: 01-089-1545
[50] jcpds: 00-009-0232
[51] J. A. Bearden and A. F. Burr, "Reevaluation of X-ray atomic energy levels," Rev. Mod. Phys. 39(1), 125–142 (1967 https://doi.org/10.1103/RevModPhys.39.125
[52] Hayashi, K.; Uno, T. Reflective Mask Blank for Euv Lithography. U.S. Patent 13/346,026, 3 May 2012.
[53] H.-C. Su et al., "Comparison between the atomic force microscopy and x-ray reflectivity on the characterization of the roughness of a surface," in Testing, Reliability, and Application of Micro- and Nano-Material Systems II, N. Meyendorf, G. Y. Baaklini, and B. Michel, Eds., SPIE (2004). https://doi.org/10.1117/12.539761
[54] S.-M. Wu et al., "Sputtering yields of Ru, Mo, and Si under low energy Ar+ bombardment," J. Appl. Phys. 106(5), 054902 (2009) https://doi.org/10.1063/1.3149777
[55] R. V. Stuart and G. K. Wehner, "Sputtering yields at very low bombarding ion energies," J. Appl. Phys. 33(7), 2345–2352 (1962) https://doi.org/10.1063/1.1728959